Ma Ying Juan (Orcid ID: 0000-0003-2584-7091)
Fang Xiaohua (Orcid ID: 0000-0002-6584-2837)
Halekas Jasper, S. (Orcid ID: 0000-0001-5258-6128)
Xu Shaosui (Orcid ID: 0000-0002-5121-600X)
Russell Christopher T. (Orcid ID: 0000-0003-1639-8298)
Luhmann Janet, G (Orcid ID: 0000-0003-0626-9353)
Toth Gabor (Orcid ID: 0000-0002-5654-9823)
Lee Christina, O. (Orcid ID: 0000-0002-1604-3326)
Dong Chuanfei (Orcid ID: 0000-0002-8990-094X)
Espley Jared, Randolph (Orcid ID: 0000-0002-6371-9683)
Mitchell David, L. (Orcid ID: 0000-0001-9154-7236)
Jakosky Bruce, M. (Orcid ID: 0000-0002-0758-9976)

The Impact and Solar Wind Proxy of the 2017 September ICME Event at Mars

Yingjuan Ma[1], Xiaohua Fang[2], J. S. Halekas[3], Shaosui Xu[4], Christopher T. Russell[1], Janet G. Luhmann[4], Andrew F. Nagy[5], G. Toth[5], Christina O. Lee[4], Chuanfei Dong[6], J. R. Espley[7], J. McFadden[4], D. Mitchell[4], and B. M. Jakosky[2]

[1]Department of Earth Planetary and Space Sciences, UCLA, Los Angeles, CA, USA
[2]Laboratory for Atmospheric and Space Physics, University of Colorado, Boulder, CO, USA
[3]Department of Physics and Astronomy, University of Iowa, Iowa City, IA, USA
[4]Space Sciences Laboratory, University of California, Berkeley, California, USA
[5]Department of Atmospheric, Oceanic and Space Sciences, University of Michigan, Ann Arbor, MI, USA
[6]Department of Astrophysical Sciences and Princeton Plasma Physics Laboratory, Princeton University, Princeton, NJ, USA
[7]NASA Goddard Space Flight Center, Greenbelt, MD, USA

Key points:
1. A solar wind proxy method is developed and validated for the 2017 September ICME event.
2. Time-dependent MHD model reproduces detailed structures observed by MAVEN for the ICME event.
3. Model predicts drastic variation of plasma boundaries and large enhancement of ion loss rates during the event.

Abstract
We study a large ICME event impacting Mars in mid-September 2017 numerically. During this time period, MAVEN remained inside the Martian bow shock, and therefore could not measure the solar wind directly. We first simulate the event using three steady-state cases with estimated solar wind conditions, and find that these cases were able to reproduce the general features observed by MAVEN. However, these time-stationary runs cannot capture the response of the system to large variations in the solar wind associated with the event. To address this question, we derive a solar wind proxy based on MAVEN observations in the sheath region and their

comparison with steady-state MHD model results. The derived solar wind proxy is then used to drive a time-dependent MHD model, and we find that the data-model comparison is greatly improved, especially in the magnetosheath. We are able to reproduce some detailed structures observed by MAVEN during the period, despite the lack of a direct measurement of the solar wind, indicating the derived solar wind conditions are reliable. Finally, we examine in detail the impact of the event on the Martian system: including variations of the three typical plasma boundaries and the ion loss rates. Our results show that these plasma boundary locations varied drastically during the event, and the total ion loss rate was enhanced by more than an order of magnitude.

Section 1 Introduction

Mars does not have a strong global magnetic field, with only non-uniformly distributed crustal magnetic fields [*Acuna et al.*, 1999]. As a result, it interacts with the solar wind in a much more direct way, similar to other unmagnetized obstacles such as Venus, with some complications caused by crustal magnetic anomalies. Solar wind conditions play important roles in controlling the locations of plasma boundaries around Mars [*Edberg et al.*, 2009] and ion escape rate from the planet [*Ramstad et al.*, 2015]. Space weather events, such as interplanetary coronal mass ejections (ICMEs), are associated with significantly disturbed solar wind conditions, such as enhancement of the solar wind dynamic pressure and IMF direction changes. Thus their influences on plasma environments and the atmosphere of Mars have been the subject of many studies [*Crider et al.*, 2005; *Dubinin et al.*, 2009; *Haider et al.*, 2009; *Edberg et al.*, 2010; *Opgenoorth et al.*, 2013; *Morgan et al.*, 2014]. However, most of the early event studies were restricted due to limited spacecraft coverage or limited plasma instruments on board.

The ongoing Mars Atmosphere and Volatile EvolutioN (MAVEN) mission carries a comprehensive plasma instrument package, and covers most of the plasma regions during the majority of its orbits, enabling a comprehensive evaluation of the impact of space weather events. Even though MAVEN has operated mostly during moderate to quiet solar activity cycle phases, it has observed quite a few strong ICMEs, of which the 8 March 2015 ICME event has been extensively studied [*Jakosky et al.*, 2015; *Dong et al.*, 2015; *Curry et al.*, 2015; *Hara et al.*, 2016], with both MAVEN measurements and multiple time-stationary numerical simulations. The 2015 March ICME was also examined in detail based on a time-dependent MHD simulation [*Ma et al.,* 2017], using time-varying upstream solar wind conditions observed by MAVEN. The large variations of the ionosphere and magnetosphere in response to the disturbed solar wind conditions were for the first time reproduced by the model, which also provided a quantitative description of the variation of the ion loss rates for the ICME event.

On 10 September 2017, MAVEN observed an X-class solar flare affecting Mars, shortly followed by a fast interplanetary coronal mass ejection (ICME) [*Lee et al.*, 2018], providing another great opportunity to advance our understanding of space weather events and their impact

2

on Mars. In this paper, we examine in detail the impact of the 2017 September ICME event on the Martian system using numerical simulations to interpret the global responses. The numerical method is described in section 2. Results and comparisons with steady-state cases are presented in section 3, followed by a description of a solar wind proxy derived for the time period (section 4) and the results from the related time-dependent MHD model (section 5). The paper concludes with a brief summary and discussion.

Section 2. Model description

A multi-species single-fluid MHD model of the Mars-solar wind interaction is used in this study in both steady-state mode [*Ma et al.*, 2004] and time-dependent mode [*Ma et al.*, 2015, 2017]. This model has been described in detail in *Ma et al.* [2004] and *Ma et al.* [2015]. It includes both a Mars crustal field description and the major Mars atmospheric gases from which Mars O^+, O_2^+ and CO_2^+ ions are produced by photoionization, electron impact ionization, and charge exchange. Some recent updates include the ability to calculate optical depth based on the Chapman function [*Ma et al.,* 2015], and to use a more recent crustal field model of *Morschhauser et al.* [2014] in the MHD model. The steady-state model results have been previously validated using Viking observations [*Ma et al.*, 2004], while the time-dependent MHD model results have been compared with Mars Global Surveyor (MGS) [*Ma et al.*, 2014] and MAVEN for both quiet [*Ma et al.*, 2015] and disturbed solar wind conditions [*Ma et al.*, 2017].

In steady-state mode, the solar wind conditions and planet orientation are kept constant. The code uses a local time-stepping scheme, and each grid cell is advanced with the locally stable time step, so that the solution can quickly converge to a quasi-steady state. This provides an efficient way to obtain a general understanding of the solar wind interaction process under different driving parameters (e.g. solar wind density, velocity, IMF strength and EUV flux). In cases when the solar wind conditions are highly variable and the system response time is of interest, it is more appropriate to use the model in the time-dependent mode. The time-dependent mode requires more intense computational resources, as the time step allowed in this mode is fairly small, ranging between $\Delta t= 0.005 – 0.01$ s, largely depending on the upstream solar wind velocity. In addition to the time-varying solar wind conditions, this model can also take into account the rotation of the crustal magnetic field [*Ma et al.*, 2014; *Fang et al.*, 2015, 2017].

The spherical grid structure and resolution are the same as in *Ma et al.* [2017], with 10 km radial resolution in the ionosphere. The calculation is done in Mars Solar Orbital (MSO) coordinates: with the X axis pointing from Mars toward the Sun, the Y axis pointing opposite the direction of Mars' orbital velocity perpendicular to X, and the Z axis completing the orthogonal coordinate. In September 2017, Mars was located at 60 degrees solar longitude near the northern summer solstice. The corresponding subsolar latitude is about 21.7 degrees, and the Mars rotational axis in MSO is given by: [0.37, 0.21, 0.905]. The outputs include the vector magnetic fields and

3

plasma moments (density, velocity and temperature) at the grid points. Mars ion escape rates are derived by integrating the planetary ion fluxes exiting through a spherical surface at 6 R_M.

Section 3: Results from three steady-state cases

During the ICME event, MAVEN orbits were located entirely inside the Martian bow shock, thus no direct solar wind measurement is available. Meanwhile, Mars EXpress (MEX) did go out in the solar wind for some time periods, but MEX science operations were turned off due to power restrictions [*Lee et al.,* 2018]. Three steady-state cases are first simulated using estimated solar wind conditions as listed in Table 1. The solar wind density and speed were estimated based on Solar Wind Ion Analyzer (SWIA) [*Halekas et al.*, 2015a] observations of penetrating proton flux near periapsis [*Halekas et al.*, 2015b, 2017]. The IMF strength and clock angle are estimated according to magnetometer (MAG) [*Connerney et al.*, 2015a, 2015b] observations in the sheath region. Case 1 represents the quiet solar wind condition prior to the ICME arrival; Cases 2 and 3 correspond to the disturbed solar wind conditions associated with the ICME at its early and late phases, respectively.

The MAVEN observations from the SWIA, MAG and the SupraThermal And Thermal Ion Composition (STATIC) [*McFadden et al.,* 2015] during the first 10-hour time period on 13 September 2017 are compared with the steady-state model results in Figure 1a (Figure 1b shows comparison with a time-dependent MHD run and will be discussed later in section 5). The results from three steady-state cases are combined together, with each case representing a certain time period as specified in Table 1. Before the ICME shock arrival (indicated by the vertical purple dashed line marked as T1, corresponding to 2:52 UT), results from the quiet case (Case 1) agree best with MAVEN observations. After T1, solar wind pressure and IMF strength were largely enhanced and such conditions are better captured by Case 2. The IMF direction reversed from the "toward" sector to the "away" sector around T2 (second vertical line, ~ 5:10 UT). After T2, Case 3 reproduces results that are closest to the observations. Over the time period, the crustal field contribution is insignificant along the MAVEN orbit, with a peak value of 50 nT near the second periapsis, less than half of the total field strength. Corresponding ion escape rates for the three cases are calculated and listed in Table 1. The Mars atmospheric ion loss rates are significantly enhanced after the ICME arrival: the total ion loss rate increased to 4.7 and 12.2 times more than the quiet case for Cases 2 and 3, respectively.

The overall features of the plasma density, velocity, magnetic field strength and the three field components are all reasonably captured by the three steady-state simulations. But there are also some notable discrepancies. For example, the plasma velocity is over-predicted by Case 2 between 4:00 and 5:00 UT, and the proton density is overestimated by Case 3 between 5:40 UT and 7:00 UT. As the solar wind condition is highly variable during the ICME event, the time-

4

stationary model runs could not capture the observed variability and fluctuations in plasma and field measurements.

Section 4: Deriviation of the solar wind conditions

To quantify the system response to the highly variable solar wind conditions associated with the ICME, a time-dependent run with realistic solar wind input conditions is needed. To overcome the difficulty of lacking direct solar wind measurements, we developed a method to derive the upstream solar wind conditions based on MAVEN observations in the magnetosheath region.

Even though the relation between solar wind plasma conditions and sheath plasma conditions is not exactly linear, sheath plasma conditions normally have a direct correlation with the solar wind conditions. For a certain Mach number condition, when solar wind density increases, we expect the proton density inside the sheath to rise; similarly, when the upstream solar wind velocity is enhanced, the plasma velocity in the sheath region becomes greater. So, we can estimate instant solar wind conditions (density, velocity and magnetic field strength) using the observed plasma conditions adjusted by a compression (or slow down) factor as expressed in the following equations:

$$n_{sw} = n_{obs(H+)} / (n_{model(H+)} /n_{sw0}) \tag{1}$$
$$U_{Xsw} = U_{Xobs(H+)} / (U_{Xmodel(H+)}/U_{Xsw0}) \tag{2}$$
$$B_{IMF} = B_{obs} /(B_{model}/B_{IMF0}) \tag{3}$$

Here n_{sw0}, U_{Xsw0} and B_{IMF0} are the input solar wind conditions of any of the steady-state runs, and $n_{model(H+)}$, $U_{Xmodel(H+)}$ and B_{model} are outputs of the corresponding run at MAVEN locations. The instantaneous solar wind density (n_{sw}) is estimated to be the observed proton density $n_{obs(H+)}$ adjusted by a compression factor ($n_{model(H+)} /n_{sw0}$). So, the solar wind density n_{sw} would be higher (lower) than n_{sw0}, if the observed plasma density $n_{obs(H+)}$ is larger (smaller) than model prediction $n_{model(H+)}$. The underlying assumption is that the normalized density at any given location in the sheath region is nearly a constant. Such an assumption should work well if the observations and model predictions are similar, meaning that the actual solar wind conditions are not largely different from the input solar wind conditions of the model. In cases when the fast Mach number changes substantially, the results from the proxy method may not be very accurate. Similarly, we can estimate the solar wind velocity component U_{Xsw} and IMF strength B_{IMF} using equations (2) and (3). Note that this method does not work inside the induced magnetosphere where the plasma flow is significantly slowed down and a large number of Mars ions are being picked up. So we only apply the proxy when $(U_{Xmodel(H+)}/U_{Xsw0})$ is larger than 0.7 and at altitudes greater than 1600 km.

5

We assume the upstream IMF B_X component is zero and the IMF clock angle is the same as the magnetic field measurement in the sheath region. The IMF clock angle is defined as the angle of the field vector in the Y_{MSO}-Z_{MSO} plane where $0°$ is along $+Y_{MSO}$ and counted counterclockwise. It has been found that the clock angle in the dayside sheath region can provide a good proxy for the upstream IMF [*Fang et al.*, 2018]. The assumption works the best for low solar zenith angles at high altitude. In the worst case, the error is about 20 degrees, considering the fact that the SZAs of MAVEN orbits are between 62-117 degrees during the event and we only use the proxy above 1600 km altitude. Also, we assume the solar wind flow is only along the X direction, and U_Y and U_Z are neglected.

We use one-minute average data when deriving the solar wind proxy. Also, we combine the solar wind proxies from the three steady-state cases with each case covering the time period when it best agrees with the MAVEN observations. In addition, when deriving the time series of the solar wind proxy data, a time shift is included to take into account the propagation time from the outer boundary of the simulation ($X_0 = 8\ R_M$) to the spacecraft location (X_{SC}) where the measurement was made. Specifically, the delay time is calculated as:

$$\Delta t = (X_0 - X_{SC}) / U_{XSW} \tag{4}$$

The above equation only roughly estimates the time-delay as the slowdown of the plasma inside the shock is neglected. So, the actual delay time should be a little longer, but the error should be fairly small as we only apply the proxy when the sheath flows are faster than 0.7 of the solar wind speed.

Using the method described above, we converted MAVEN measurements in the sheath region to solar wind conditions. The derived solar wind proxy is plotted in Figure 2 together with MAVEN SWIA and MAG observations. As can be seen from panels b and d, in most of the regions, the derived solar wind density (and magnetic field strength) is notably smaller than the sheath proton density (and field magnitude) as observed by MAVEN, due to the compression of the plasma density (and magnetic field) across the shock. Panel c shows the derived solar wind speed as somewhat larger than the measurements, consistent with the slowdown of the solar wind plasma across the shock. The predicted solar wind density varies between 1.7 to 16 cm^{-3}, velocity ranges from 300 to 880 km/s, and magnetic field strength changes between 1.1 to 18.5 nT during the 10-hour time period. These large variations of the solar wind conditions during the time period are also shown in Figure 3, panels 1, 3, and 5. The solar wind dynamic pressure changes from 1.0 nPa from pre-ICME conditions to a peak value of 20.8 nPa around 8UT, with a peak fast Mach number (Mf) of 8.2 at a similar time.

Even though MAVEN was inside the Martian bow shock during the entire period, the SWIA was in the solar wind mode during some time periods: 3:40-3:50, 8:50-9:20, and 9:55-10:05 UT. In this mode of SWIA operation, its field of view is focused on the solar direction. As a result, SWIA missed part of the particle distribution of the deflected sheath plasma in the onboard

6

moments. Those data are neglected when deriving the solar wind density and velocity (see Figure 2b and 2c). Also note that the ICME event was associated with solar energetic particles which may produce some artificial background in the SWIA detector. As the background counts are roughly uniformly distributed over all energies and angles, this results in a higher density (because more counts are added) and a lower bulk velocity (because extra counts are spread over all angles). It is estimated that the density could be overestimated by as much as 1 cm^{-3} and the flow velocity could be up to 100 km/s lower when the ambient plasma density is low.

Section 5: Time-dependent MHD model results
We next use the derived solar wind proxy to drive the time-dependent simulation to quantify the impact of the ICME on the Martian plasma environment. In the time-dependent run, the time-varying solar wind conditions propagate into the simulation domain from the upstream boundary ($8R_M$), and the data gap in the proxy is filled in using linear interpolation, except near the ICME shock arrival, a plasma jump condition was specified (see redlines in Figure 2b-2g).

The comparison of the time-dependent model results with MAVEN observations in Figure 1b is significantly better than its steady model counterpart in Figure 1a, especially in the sheath region. As can be seen from panels b2 and b3, variations in proton density and U_X components of SWIA are closely followed by the time-dependent model results, much improved from the steady-state cases. There are still some discrepancies around 4:20 UT in U_Y and U_Z components, likely due to the fact that we assume that the solar wind flow is exactly aligned with the X axis, which might not be the case during this particular time. The sharp enhancement of the magnetic field strength at the ICME shock arrival is well captured by the model at the right time with the correct magnitude, as shown in panel b4. The magnetic field rotation between 5:00-6:00 UT is also well reproduced by the model (see panels b5-b7). The B_X component is well reproduced despite the fact that the IMF B_X component is neglected when deriving the solar wind proxy. This indicates that in the sheath region, the measured B_X is largely due to the draping of the magnetic field lines. The good model-data comparison clearly demonstrates that the solar wind proxy derived using the method (described in section 4) is quite reliable for this event.

Detailed responses of the Martian system to the ICME event is examined based on the time-dependent MHD model results. Three typical plasma boundaries are determined using the following criteria:
1. ICB (ion composition boundary): where planetary ions become dominant over solar wind protons;
2. IMB (induced magnetosphere boundary): where the magnetic field pressure becomes the dominant pressure over thermal pressure and dynamic pressure;
3. BS (bow shock): where the plasma flow speed becomes slower than the fast magnetosonic speed.

7

These plasma boundaries are calculated every minute along the subsolar line based on model results as shown in Figure 3. The color plot in panel b shows the variation of plasma flow speed along the subsolar line in response to changes of the solar wind flow, together with BS locations marked by the black curve. BS locations vary between 1.40-1.80 R_M, anti-correlating with fast Mach number (Mf) (see panel a). Panel d shows the time-variation of magnetic field strength (color) together with IMB locations in black curve. The IMB locations vary between 1.05-1.66 R_M, showing a clear dependence on the IMF strength (see panel c). Panel f shows the time-variation of electron number density (color) together with ICB locations (in black). The ICB locations change between 292 km - 462 km altitude, weakly anti-correlating with solar wind density and pressure (see panel e). The time-dependent ion loss rates are shown in the bottom panel (g). The total ion escape rate increases from 1.7×10^{24} to 3.5×10^{25} s^{-1}, enhanced by more than 20 times, mostly controlled by the solar wind dynamic pressure. The peak value is about 60% larger than predicted by Case 3 of the steady-state cases. For the majority of the times after the ICME shock arrival, the ion loss is dominated by O_2^+. The contribution of O^+ becomes comparable and overtakes that of O_2^+ for a very short time period when the solar wind density is relatively high. The solar wind conditions for this event were more disturbed as compared with the 8 March 2015 ICME event, with a higher peak solar wind pressure (20 nPa vs 15 nPa), and a larger variation of Mach number. As a result, the plasma boundaries showed large variations in this event, and the related total ion loss rate was enhanced by a larger factor (21 vs 10) [*Ma et al.*, 2017].

The magnetic field topology response to the event is also examined in detail by Xu et al. [2018], in connection with interpretations of the Solar Wind Electron Analyzer (SWEA, [*Mitchell et al.*, 2016]) observations. Both SWEA observations and the time-dependent MHD model results suggest that the IMF penetrates deeper into the ionosphere due to the enhanced solar wind dynamic pressure, a response that is also partly responsible for the enhanced Mars ion losses.

Section 6. Discussion and conclusions:
We have used a multi-species single fluid MHD model to study the 2017 September ICME event based on both steady-state cases and time-dependent mode runs. The three steady-state cases are compared with MAVEN in-situ time series observations of the plasma and magnetic field along the S/C orbit. Each steady-state case captures the main features of the observations for a certain period, corresponding to pre-ICME, early and late phases, respectively. Results from steady-state runs are also used to derive a solar wind proxy, which is tested using a time-dependent MHD model. Comparison between the MAVEN plasma and field observations and the time-dependent MHD model results along MAVEN's orbit show that the agreement is greatly improved compared to the steady state runs, especially in the magnetosheath region. This clearly demonstrates that the solar wind density, velocity (x component), magnetic field strength and clock angle can be determined quite accurately using the method, proving a viable alternative to use for simulations when actual upstream observations are not available. The data-validated

8

time-dependent simulation results in turn provide global information on Mars' response to the local interplanetary conditions.

As the steady state runs are time-efficient, this provides an in-expensive method to infer the solar wind conditions from magnetosheath observations. However, there are still some caveats in the proxy, e.g. some solar wind parameters such as B_X, U_Y, and U_Z are currently neglected. The solar wind proxy method can certainly be further improved. For example, in addition to sheath observations, the magnetic field measurements inside the MPB region can also be used to constrain the solar wind conditions, as the peak of the magnetic field strength should be a good indicator of the solar wind dynamic pressure, and the magnetic field direction there can be used to infer the clock angle. However, such information is not as straightforward to relate to upstream conditions as the sheath measurements. In addition, the time delay needs to be properly included, because the plasma flow slows down significantly due to the mass loading by the planetary ions. We will try to address these caveats and improve the solar wind proxy method in our future studies.

The time-dependent MHD model results are examined to quantify the response of the Martian system. It is found that locations of different plasma boundaries are controlled by different solar wind parameters. We also infer that there is a significant enhancement of the Mars ion loss rates. Compared with the 8 March 2015 ICME event, the solar wind conditions for this event were more disturbed. As a result, the plasma boundaries showed larger variations with more enhanced total ion loss rate. This finding further reinforces the idea that space weather effects can have a significant effect on the Mars atmosphere escape. The full range of these enhancements can be better determined by similar analyses of additional, even larger, events.

References
Acuna, M. H., et al. (1999), Global distribution of crustal magnetization discovered by the Mars Global Surveyor MAG/ER experiment, Science, 284, 790–793.

Connerney, J.E.P., Espley, J.R., Lawton, P., Murphy, S., Odom, J., Oliversen, R., & Sheppard, D. (2015a). The MAVEN magnetic field investigation.*Space Sci. Rev.,* vol. 195, no. 1, pp. 257-291, doi: 10.1007/s11214-015-0169-4.

Connerney, J.E.P., Espley, J.R., DiBraccio, G.A., Gruesbeck, J.R., Oliversen, R.J., Mitchell, D.L., Halekas, J., Mazelle, C., Brain, D.A., & Jakosky, B.M. (2015b). First results of the

MAVEN magnetic field investigation. *Geophys. Res. Lett., 42,* 8819–8827, doi:10.1002/2015GL065366.

Crider, D. H., J. Espley, D. A. Brain, D. L. Mitchell, J. E. P. Connerney, and M. H. Acuña (2005), Mars Global Surveyor observations of the Halloween 2003 solar superstorm's encounter with Mars, *J. Geophys. Res.*, **110**, A09S21, doi:10.1029/2004JA010881.

Curry, S. M., et al. (2015), MAVEN first results: The response of pick-up ions to the March 8th, 2015 ICME, *Geophys. Res. Lett.*, **42**, doi:10.1002/2015GL065304.

Dong, C., et al. (2015), Multifluid MHD study of the solar wind interaction with Mars' upper atmosphere during the 2015 March 8th ICME event, *Geophys. Res. Lett.*, **42**, doi:10.1002/2015GL065944.

Dubinin, E. et al., Ionospheric storms on Mars: Impact of corotating interaction region. Geophys. Res. Lett. 36, L01105 (2009). doi: 10.1029/2008GL036559

Edberg, N. J. T., et al. (2009), Rosetta and Mars Express observations of the influence of high solar wind dynamic pressure on the Martian plasma environment, *Ann. Geophys.*, **27**, 4533–4545, doi:10.5194/angeo-27-4533-2009.

Edberg, N. J. T., H. Nilsson, A. O. Williams, M. Lester, S. E. Milan, S. W. H. Cowley, M. Fränz, S. Barabash, and Y. Futaana (2010), Pumping out the atmosphere of Mars through solar wind pressure pulses, Geophys. Res. Lett., 37, L03107, doi:10.1029/2009GL041814.

Haider, S. A., M. A. Abdu, I. S. Batista, J. H. Sobral, E. Kallio, W. C. Maguire, and M. I. Verigin (2009), On the responses to solar X-ray flare and coronal mass ejection in the ionospheres of Mars and Earth, *Geophys. Res. Lett.*, **36**, L13104, doi:10.1029/2009GL038694.

Fang X., Y. Ma, J.G Luhmann, Y. Dong, D.A. Brain, D.M. Hurley, C. Dong, C.O.-Y. Lee, and B.M. Jakosky (2018), The morphology of the solar wind magnetic field draping on the dayside of Mars and its variability, *Geophys. Res. Lett.*, 45, doi:10.1002/2018GL077230.

Fang, X., Y. Ma, D. Brain, Y. Dong, and R. Lillis (2015), Control of Mars global atmospheric loss by the continuous rotation of the crustal magnetic field: A time-dependent MHD study, *J. Geophys. Res. Space Physics*, 120, 10,926–10,944, doi:10.1002/2015JA021605.

Fang, X., et al. (2017), The Mars crustal magnetic field control of plasma boundary locations and atmospheric loss: MHD prediction and comparison with MAVEN, *J. Geophys. Res. Space Physics*, 122, 4117–4137, doi:10.1002/2016JA023509.

Y. Futaana et al., Mars Express and Venus Express multi-point observations of geoeffective solar flare events in December 2006. Planet. Space Sci. 56, 873–880 (2008). doi: 10.1016/j.pss.2007.10.014

Halekas, J., E. Taylor, G. Dalton, G. Johnson, D. Curtis, J. McFadden, D. Mitchell, R. Lin, and B. Jakosky (2015a), The solar wind ion analyzer for MAVEN, *Space Sci. Rev.*, **195**, 125–151, doi:10.1007/s11214-013-0029-z.

Halekas, J. S., et al. (2015b), MAVEN observations of solar wind hydrogen deposition in the atmosphere of Mars, Geophys. Res. Lett., 42, 8901–8909, doi:10.1002/2015GL064693.

Halekas, J. S., et al. (2017), Structure, dynamics, and seasonal variability of the Mars-solar wind interaction: MAVEN Solar Wind Ion Analyzer in-flight performance and science results, J. Geophys. Res. Space Physics, 122, 547–578, doi:10.1002/2016JA023167.

Hara, T., et al. (2016), MAVEN observations of magnetic flux ropes with a strong field amplitude in the Martian magnetosheath during the ICME passage on 8 March 2015, *Geophys. Res. Lett.*, **43**, 4816–4824, doi:10.1002/2016GL068960.

Jakosky, B. M., et al (2015), MAVEN observations of the response of Mars to an interplanetary coronal mass ejection, *Science*, 350, aad0210-1-aad0210-7, doi:10.1126/science.aad0210.

Lee et al., Observations and Impacts of the 10 September 2017 Solar Events at Mars: An Overview, 2018, GRL, this issue, under review.

Luhmann, J. G., W. T. Kasprzak, and C. T. Russell (2007), Space weather at Venus and its potential consequences for atmosphere evolution, *J. Geophys. Res.*, **112**, E04S10, doi:10.1029/2006JE002820.

Luhmann, J. G., et al. (2008), Venus Express observations of atmospheric oxygen escape during the passage of several coronal mass ejections, *J. Geophys. Res.*, **113**, E00B04, doi:10.1029/2008JE003092.

Ma, Y., A. F. Nagy, I. V. Sokolov, and K. C. Hansen (2004), Three-dimensional, multispecies, high spatial resolution MHD studies of the solar wind interaction with Mars, *J. Geophys. Res.*, **109**, A07211, doi:10.1029/2003JA010367.

Ma, Y. J., X. Fang, A. F. Nagy, C. T. Russell, and G. Toth (2014), Martian ionospheric responses to dynamic pressure enhancements in the solar wind, *J. Geophys. Res. Space Physics*, **119**, 1272–1286, doi:10.1002/2013JA019402.

Ma, Y. J., C. T. Russell, X. Fang, Y. Dong, A. F. Nagy, G. Toth, J. S. Halekas, J. E. P. Connerney, J. R. Espley, P. R. Mahaffy, et al. (2015), MHD model results of solar wind

interaction with Mars and comparison with MAVEN plasma observations, Geophys. Res. Lett., 42, 9113–9120, doi:10.1002/2015GL065218.

Ma, Y. J., et al. (2017), Variations of the Martian plasma environment during the ICME passage on 8 March 2015: A time-dependent MHD study, J. Geophys. Res. Space Physics, 122, 1714–1730, doi:10.1002/2016JA023402.

McFadden, J., et al. (2015), The MAVEN Suprathermal and Thermal Ion Composition (STATIC) instrument, *Space Sci. Rev.*, **195**, 199, doi:10.1007/s11214-015-0175-6.

Mitchell, D. L., et al. (2016), The MAVEN Solar Wind Electron Analyzer, *Space Sci. Rev.*, **200**, 495–528, doi:10.1007/s11214-015-0232-1.

Morgan, D. D., et al. (2014), Effects of a strong ICME on the Martian ionosphere as detected by Mars Express and Mars Odyssey, *J. Geophys. Res. Space Physics*, **119**, 5891–5908, doi:10.1002/2013JA019522.

Opgenoorth, H. J., D. J. Andrews, M. Fränz, M. Lester, N. J. T. Edberg, D. Morgan, F. Duru, O. Witasse, and A. O. Williams (2013), Mars ionospheric response to solar wind variability, *J. Geophys. Res. Space Physics*, **118**, 6558–6587, doi:10.1002/jgra.50537.

Ramstad, R., S. Barabash, Y. Futaana, H. Nilsson, X.-D. Wang, and M. Holmström (2015), The Martian atmospheric ion escape rate dependence on solar wind and solar EUV conditions: 1. Seven years of Mars Express observations, J. Geophys. Res. Planets, 120, 1298–1309, doi:10.1002/2015JE004816.

Toth, G., et al. (2012), Adaptive numerical algorithms in space weather modeling, *J. Comput. Phys.*, **231**(3), 870–903, doi:10.1016/j.jcp.2011.02.006.

Xu et al., Investigation of Martian magnetic topology response to 2017 September ICME 2018, GRL, accepted (manuscript # 2018GL077708, this issue)

12

Table 1. Solar wind conditions used for the three steady state cases and corresponding ion loss rates with applicable time periods.

Case No.	Case 1 (quiet)	Case 2 (early phase)	Case 3 (later phase)
Time Period*	00:01-02:52 UT	02:52-05:10 UT	05:10-10:00 UT
N_{SW} [cm^{-3}]	1.9	4.0	12.0
U_{SW} [km/s]	426	824	824
B_{IMF} [nT]	(0.0,-3.0,0.0)	(0.0, -10.0, 0.0)	(0.0, 10.0, 5.0)
O^+ loss rate [s^{-1}]	6.8×10^{23}	2.6×10^{24}	1.0×10^{25}
O_2^+ loss rate [s^{-1}]	1.0×10^{24}	5.3×10^{24}	1.0×10^{25}
CO_2^+ loss rate [s^{-1}]	9.0×10^{22}	6.5×10^{23}	1.4×10^{24}
Total loss rate [s^{-1}]	1.8×10^{24}	8.5×10^{24}	2.2×10^{25}

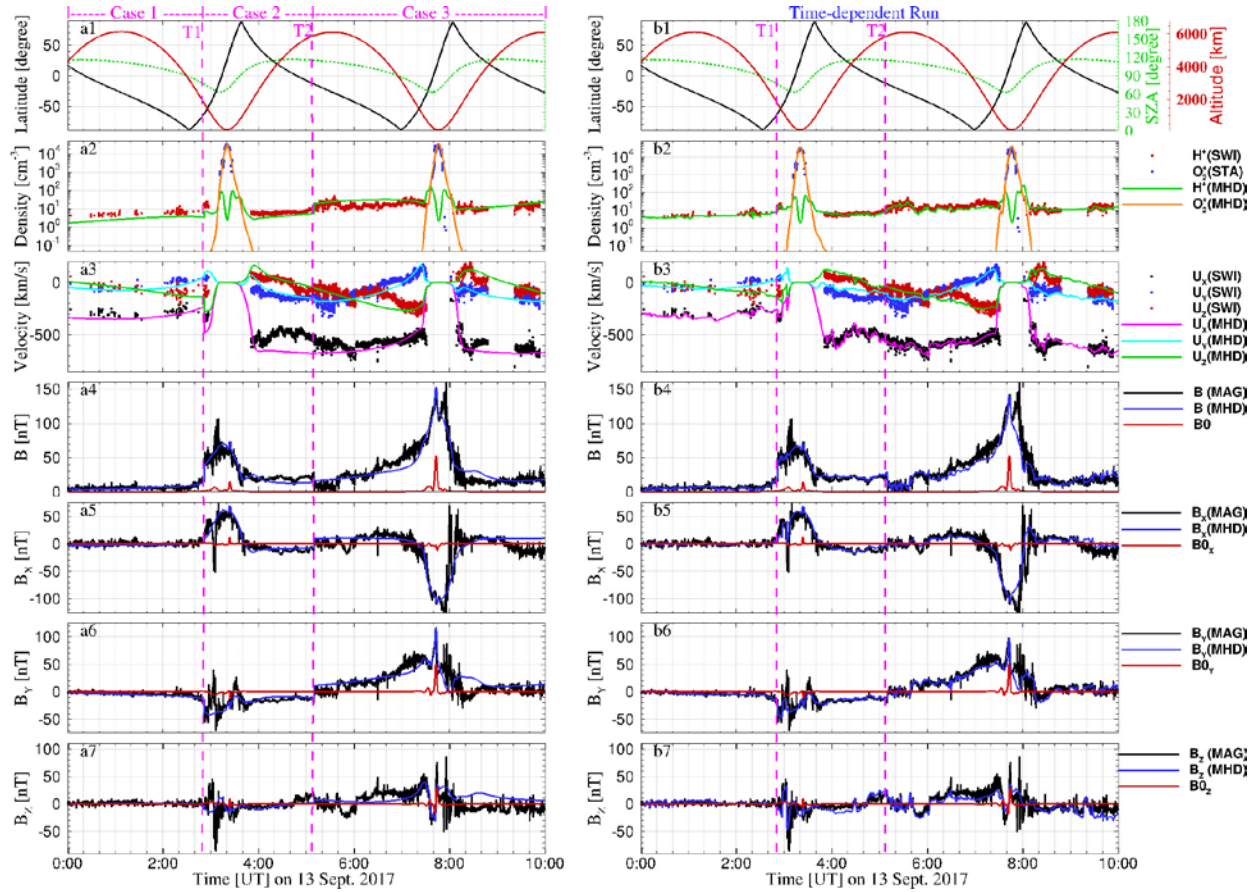*Time period corresponding to 2017-09-13.

Figure 1. MAVEN observation during the 10-hour time period and comparison with model results along MAVEN orbit for the three steady-state cases (left panels) and the time-dependent

MHD run (right panels). (a1, b1) Spacecraft trajectory information (latitude, SZA and altitude), (a2, b2) H^+ density from SWIA and MHD model, and O_2^+ density from STATIC and MHD model, (a3, b3) the three components of the plasma velocity from SWIA and MHD model, (a4, b4) magnetic field strength from MAG, MHD model and crustal field model, (a5, b5) B_X, (a6, b6) B_Y and (a7, b7) B_Z from MAG, MHD model and crustal field model in the MSO coordinates. Purple vertical lines correspond to 2:52 UT (T1) and 5:10 UT (T2), respectively.
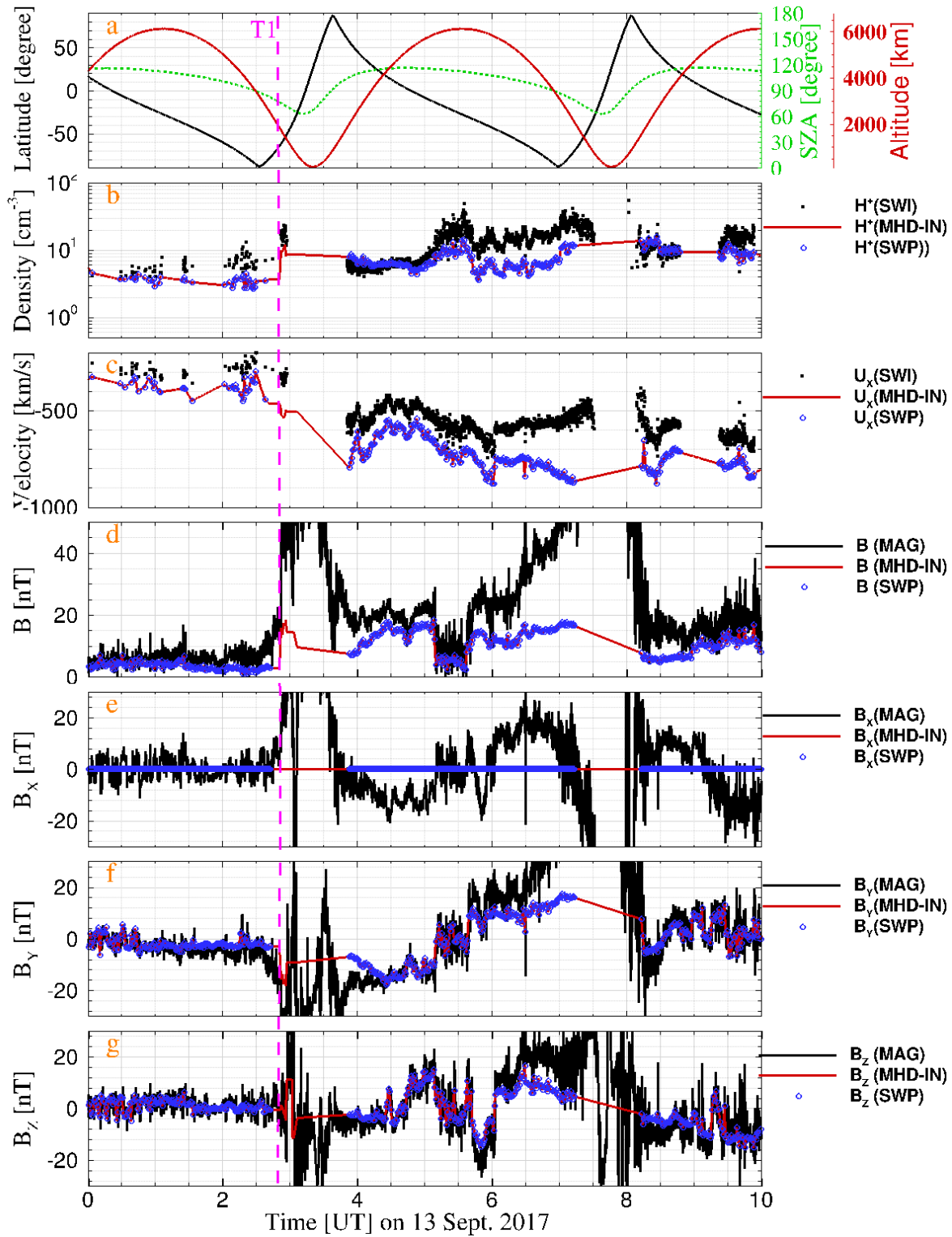
14

Figure 2. The solar wind proxy estimated based on MAVEN observations in the sheath region and the three steady-state cases with corresponding MAVEN observations as references. Panels show (a) spacecraft trajectory information in the same format as in figure 1, (b) proton density, (c) solar wind velocity along the X direction, (d) IMF strength; and the three components of the IMF (e) B_X, (f) B_Y and (g) B_Z in the MSO coordinates. In panels (b-g): black symbols are proton density and velocity observations from SWIA (panel b and c), and black lines are field strength and three components based on MAG measurements (panels d-g); blue circles are solar wind proxy derived using the method discussed in section 4; red lines are actual solar wind input to the time-dependent MHD model (labeled as MHD-IN). The purple vertical line indicates the time of the ICME shock arrival.
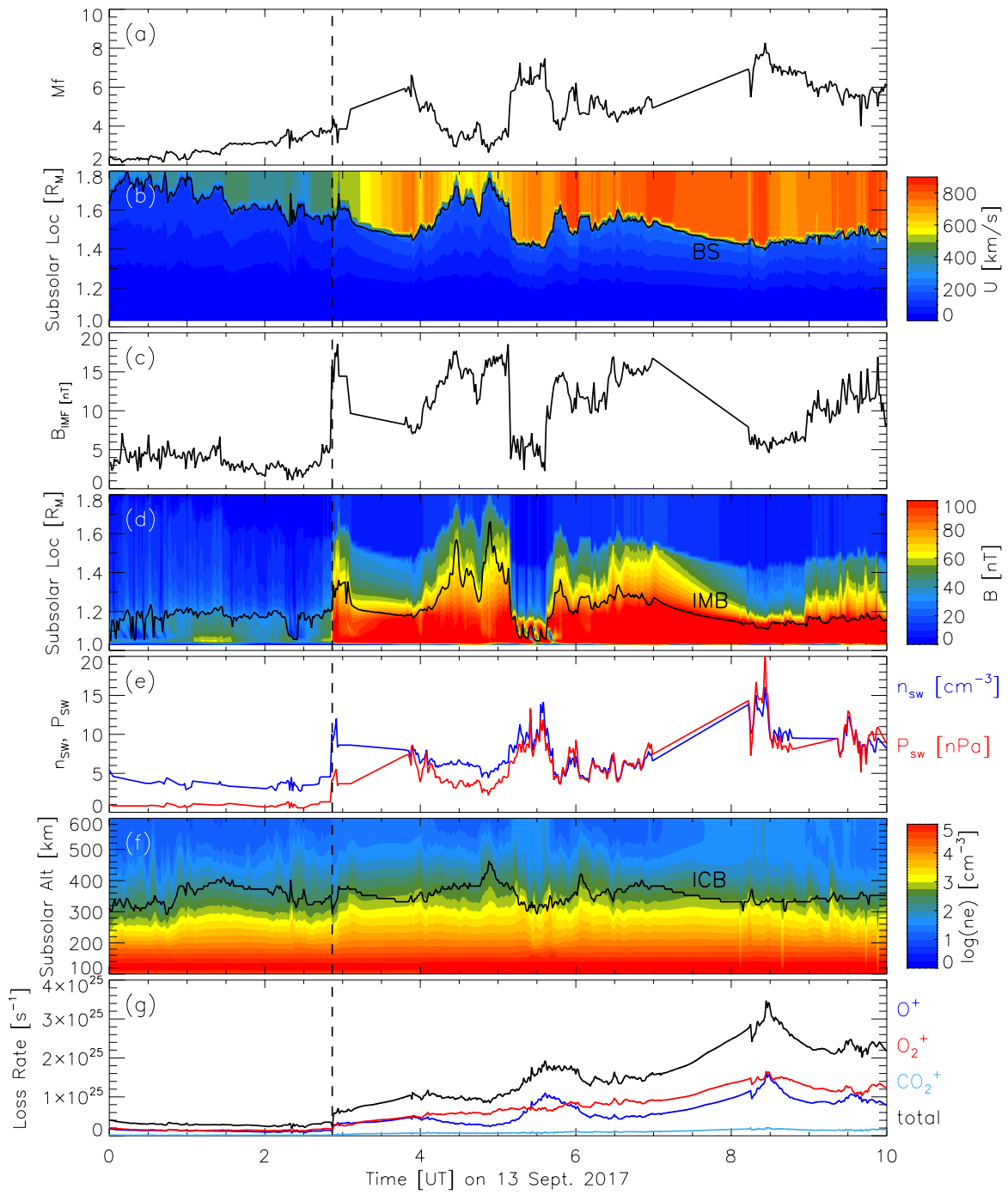
16

17

Figure 3. Variations of plasma boundaries and ion escape rates in response to the disturbed solar wind conditions during the ICME event. (a) Fast Mach number, (b) contour plot of plasma flow speed along the subsolar line with the BS locations marked by the black line, (c) IMF strength, (d) contour plot of magnetic field strength along the subsolar line with the IMB locations marked by the black line, (e) solar wind density and dynamic pressure, (f) electron number density along the subsolar line with ICB locations marked by the black line, and (g) escape rates of O^+, O_2^+, CO_2^+ and total ion loss rate, respectively. The black vertical line indicates the time of the ICME shock arrival.

18